Structural perspective on the design of selective DYRK1B inhibitors

Przemyslaw Grygier[1, 2], Katarzyna Pustelny[1], Filipe Menezes[3], Malgorzata Jemiola-Rzeminska[4], Piotr Suder[5], Grzegorz Dubin[1] and Anna Czarna[1, *]

1 Malopolska Centre of Biotechnology, Jagiellonian University, Gronostajowa 7a, 30-387 Krakow, Poland
2 Doctoral School of Exact and Natural Sciences, Jagiellonian University, Krakow, Poland
3 Helmholtz Munich, Molecular Targets and Therapeutics Center, Institute of Structural Biology, Ingolstädter Landstr. 1, 85764 Neuherberg, Germany
4 Faculty of Biochemistry, Biophysics and Biotechnology, Jagiellonian University, Krakow, Poland
5 Department of Analytical Chemistry and Biochemistry, Faculty of Materials Science and Ceramics, AGH University Cracow, A. Mickiewicza 30, 30-059 Krakow, Poland

*Corresponding author: anna1.czarna@uj.edu.pl

Abstract

DYRK1B has been recently recognized as a critical therapeutic target in oncology, metabolic syndrome, and non-alcoholic fatty liver disease. However, the development of selective inhibitors for DYRK1B, has been constrained by the lack of structural information. In this study, we employed recombinant protein production, activity assays, and crystallization to elucidate the structure of DYRK1B. We present a crystal structure of DYRK1B in complex with a known inhibitor, AZ191. For comparative analysis, we provide the crystal structure of the closely related DYRK1A kinase in complex with AZ191. Our analysis identifies a distinct binding site in the hinge region of DYRK1B, which is pivotal for the design of selective inhibitors. Quantum mechanical calculations reveal a notable difference in the accessibility of the catalytic lysine between DYRK1B and DYRK1A, suggesting a potential avenue for selective inhibitor design. These findings mark a significant advancement in the quest for specific DYRK1B inhibitors, potentially offering focused efficacy compared to the current dual-specificity inhibitors targeting both DYRK1B and DYRK1A.

Introduction

Protein phosphorylation is the most widespread post-translational modification facilitating cellular signal transduction (*1*). Deregulation of kinase signalling underlies multiple human diseases, but one of the challenges in exploring phosphorylation as a drug target arises in designing specific inhibitors addressing over 500 protein kinases of the human kinome (*2, 3*).

Aberrant activity of dual-specificity tyrosine phosphorylation-regulated kinases (DYRKs) has been linked to neurological disorders, diabetes, and cancer. DYRKs belong to a larger family of CMGC kinases which includes cyclin-dependent kinases (C), mitogen-activated protein kinases (M), glycogen synthase kinases (G), and CDC-like kinases (C). DYRK1A and DYRK1B localize mainly in the nucleus while DYRK2, DYRK3, and DYRK4 reside predominantly in the cytoplasm (*4*). The activity is regulated by autophosphorylation within the YxY motif in the activation loop (*5*). What is unique about DYRKs is their ability to autophosphorylate on tyrosine residues while phosphorylating other substrates exclusively on serine and threonine (*6*). Within the DYRK family, the DYRK1A and 1B paralogs are of major interest as drug targets. This results from their multifaceted roles in critical cellular processes that are dysregulated in various diseases. Their involvement in cell cycle regulation, tissue regeneration, and neuronal signalling pathways presents a unique opportunity to develop targeted therapies that could address mechanisms underlying cancer, diabetes, and neurodegenerative diseases.

DYRK1A and DYRK1B, as closely related paralogs, have emerged as compelling drug targets due to their integral roles in cellular homeostasis and disease pathology. DYRK1B's involvement in cancer cell proliferation and survival makes it a prime target for cancer-specific therapies. The challenge lies in developing selective inhibitors that spare DYRK1A, thereby minimizing adverse effects and enhancing treatment efficacy (*7*). In the realm of regenerative medicine, both DYRK1A and DYRK1B are pivotal for human beta cell regeneration, with their inhibition showing promise in diabetes treatment by promoting beta cell proliferation (*8, 9*). The DYRK1A gene is located at the Down Syndrome Critical Region (DSCR) of chromosome 21 and the kinase is widely considered a potential drug target in neurological disorders including Down Syndrome (DS), Alzheimer's, and Parkinson's disease (*9–12*). Furthermore, the potential of DYRK1A as a therapeutic target in neurodegenerative diseases, particularly Alzheimer's disease, underscores its relevance in neuronal function and the possibility of modulating its activity for therapeutic benefit (*13*).

DYRK1B is overexpressed in certain types of cancer where its role is better understood compared to that of DYRK1A. The overexpression of DYRK1B maintains cellular quiescence (*14*) and enhances cell survival by reducing the levels of reactive oxygen species (ROS) (*15*). It has been demonstrated that genetic depletion of DYRK1B leads to cell cycle re-entry and apoptosis (*16*). The DYRK1B gain-of-function mutation is associated with metabolic syndrome (MetS), characterized by abdominal obesity, type 2 diabetes, and hypertension (*17*). Additionally, the DYRK1B protein level increases upon DYRK1A silencing suggesting a compensatory mechanism (*18*). Although DYRK1B silencing in human islets had almost no effect on beta-cell proliferation, simultaneous silencing of DYRK1A and 1B resulted in significantly higher rates of proliferation than silencing DYRK1A alone, suggesting that dual inhibition has also its application. As such, DYRK1B is

potentially an interesting drug target for certain cancers but also in MetS. Collectively, these findings position DYRK1A and DYRK1B as versatile targets for drug discovery, with implications across oncology, diabetes management, and neurodegeneration.

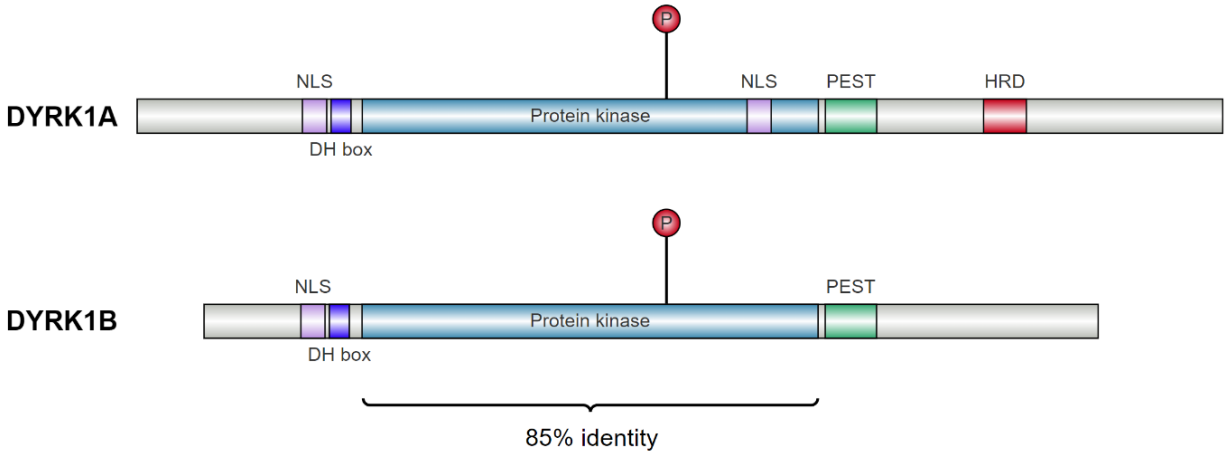

Figure 1. Schematic arrangement of domains in Human DYRK1A and DYRK1B.

In terms of inhibitor development, the conserved catalytic domain of DYRKs is the commonly considered target. Characteristic features defining the targeted active site include a glycine-rich loop and DFG motif involved in ATP binding (*19, 20*). The DFG motif adopts an "in" conformation in active kinases where the aspartic acid residue coordinates a Mg^{2+} ion bound to the β- and γ-phosphate groups of ATP. Other characteristic features include a gatekeeper residue (phenylalanine) guarding access to the ATP binding pocket (*21*) and the YxY motif determining kinase activity (*22*). In addition to the active site, the C-lobe of the catalytic domain contains a characteristic fragment (CMGC insert), which exhibits higher sequence heterogeneity compared to other regions of the kinase domain, and is involved in intermolecular interactions (*23*). The catalytic domain is flanked at the N-terminus by the DYRK homology box (DH), vital for autophosphorylation during the kinase maturation (*6, 24*) and at the C-terminus by the PEST sequence (proline, glutamic acid, serine, and threonine enriched) promoting rapid degradation (*25*) (Figure 1). DYRK1A is additionally characterized by a histidine-rich region (HRD), responsible for localization to nuclear speckles, a feature that is absent in DYRK1B. This region is characteristic of several proteins expressed in the nervous system (*26*).

Harmine is the most common inhibitor used in investigating the roles of DYRK1A and 1B in health and disease. Among other, harmine was demonstrated to inhibit tau hyperphosphorylation, a process relevant to Alzheimer's Disease pathology (*27*) and exhibits a β-cell pro-proliferative effect (*8*). However, the inhibitor is equally effective against both kinases (*28*), hindering the possibility of kinase-specific studies. Various other inhibitors of DYRKs were reported, including AZ191 (*29*), but none is specific enough to distinguish the kinases. To understand the specific effects of inhibiting each paralogue, selective inhibitors are needed. These selective inhibitors would also play a key role in the treatment of certain types of cancer (*7, 30*). However, developing selective inhibitors for closely related molecular targets is challenging and the lack of a crystal structure of DYRK1B further complicates the effort. In our work we provide the first crystal structure of

DYRK1B in complex with AZ191, which will facilitate the future development of selective inhibitors.

Results

Pivotal role of autophosphorylation in maintaining DYRK1B stability

In the process of purifying the kinase domain of DYRK1B, it was observed that a substantial fraction of the kinase aggregated in the insoluble fraction following cell lysis. This observation is particularly relevant considering the established importance of tyrosine phosphorylation within the YxY motif for the enzyme's catalytic functionality and structural stability, as documented in prior studies (*24, 31, 32*). Given this background, we hypothesized that the autophosphorylation of DYRK1B might be suboptimal when expressed in *Escherichia coli*. To investigate this, we specifically assessed the phosphorylation status of Tyr273. This was achieved through a mass spectrometry analysis conducted on the whole cell lysate.

During analysis of the whole cell lysate, the Tyr273 was clearly visible, mainly in the unphosphorylated form. Specifically, peptides: [253-277], [257-277], [157-280] and [270-280] (Uniprot ID Q9Y463) were identified based on their numerous MS/MS spectra (details in supplement: „identification report”). Among these peptides, some displayed phosphorylation at Tyr273, however the ratio between phosphopeptide and their unphosphorylated forms appeared to be low. To estimate the level of Tyr273 phosphorylation we compared peak areas of the corresponding peptides in both forms. We focused on the ions at m/z = 730.3836^{4+} (unphosphorylated [253-277]) and at m/z = 750.3749^{4+} (phosphorylated [253-277]). Identities of both peptides were verified by their fragmentation spectra to confirm the sequences and phospho-residue (Figure S1 and S2). Based on the area under the corresponding extracted ion chromatograms it can be calculated that phosphorylation efficiency was close to 14% (Figure S3). Notably, the purified DYRK1B exhibited complete phosphorylation at Tyr273, strongly suggesting that the unphosphorylated pool is unstable and thus lost during the purification process.

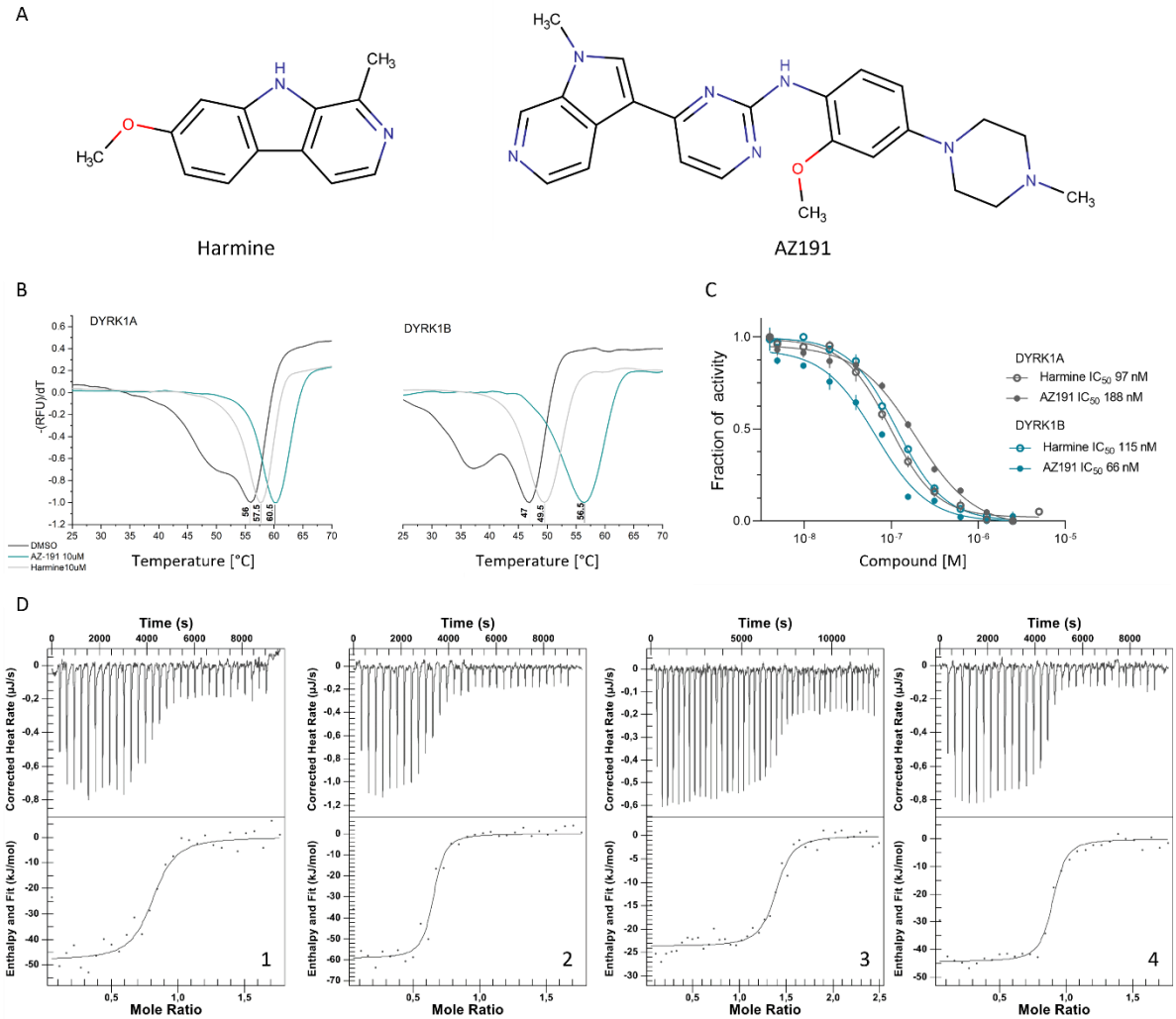

	Protein	Compound	K_d [nM]	N	ΔH [kJ mol^{-1}]	-TΔS [kJ mol^{-1}]	ΔG [kJ mol^{-1}]
1	DYRK1A	harmine	94.02	0.796 ± 0.033	-48.05 ± 3.241	7.936	-40.11
2	DYRK1B	harmine	29.38	0.630 ± 0.018	-59.15 ± 2.926	16.150	-42.99
3	DYRK1A	AZ191	54.63	1.370 ± 0.028	-23.67 ± 0.819	-17.780	-41.45
4	DYRK1B	AZ191	28.08	0.877 ± 0.014	-44.47 ± 1.341	1.362	-43.11

Figure 2. Biochemical analysis of DYRK1's interactions with harmine and AZ191. (A) Structure of harmine and AZ191. (B) Thermal denaturation curves (first derivative) of DYRK1A (left panel) and DYRK1B (right panel) kinase domains after treatment with harmine, AZ191, or DMSO as determined in the Sypro Orange dye monitored thermal shift assay. (C) Inhibitory activity of AZ191 and harmine against DYRK1A and DYRK1B determined in ADP-Glo kinase activity assay and (D) ITC.

AZ191, a potent and selective DYRK1B inhibitor, enables paralog differentiation

The thermal-shift assay revealed that the catalytic domain of DYRK1A and DYRK1B has a markedly distinct thermal profile despite the high sequence identity (over 85%). The kinase domain of DYRK1A (124-490) was more stable with a melting point of 56 °C (T_m), while the thermal denaturation of the kinase domain of DYRK1B (78-442) was observed at 47 °C (T_m) (Figure 2B). Both DYRK1s' stability was improved and their melting temperature was raised by binding of harmine or AZ191. Notably, AZ191 at 10 µM induced a remarkable 12 °C shift in T_m of DYRK1B, indicating a strong stabilizing effect. AZ191 had a less pronounced impact on DYRK1A, with only a 4 °C shift observed. Harmine, on the other hand, exhibited a moderate stabilizing effect, causing

a 1.5 °C and 2.5 °C increase in melting temperatures of DYRK1A and DYRK1B, respectively (Figure 2B). To provide a more comprehensive context for our findings regarding the significant stabilization of DYRK1B by the AZ191 inhibitor, we conducted a Cellular Thermal Shift Assay (CETSA). The thermal stability was assessed for the full-length DYRK1B expressed in HEK293 cells and treated with the inhibitor (10 μM) or DMSO. For both, DYRK1B and DYRK1B-AZ191, denaturation occurred gradually over a wide range of temperatures. However, an increased thermal stability of the full-length DYRK1B was observed following treatment with the AZ191 inhibitor (Figure S4). This provides evidence that AZ191 not only binds to and enhances the stability of the isolated kinase domain, but also the full-length DYRK1B.

The AZ191-induced thermal stabilization of DYRK1A and DYRK1B kinases prompted us to investigate the impact of the inhibitor on kinase activity profile. We employed the ADP-Glo kinase activity assay to quantify the inhibitory potency of AZ191 (IC_{50}) against DYRK1A and DYRK1B. In the assay, purified kinase domains of DYRK1A or DYRK1B (5 ng/μl) were titrated with inhibitor (5 nM – 5 μM) in the presence of ATP (100 μM) and a synthetic peptide substrate (400 μM). The ATP concentration was chosen based on the experimentally determined K_M for DYRK1A and DYRK1B of 118 μM and 105 μM respectively. AZ191 strongly inhibited DYRK1B and DYRK1A, with IC_{50} in the nanomolar range (Figure 2C). Notably, the inhibitory effect was more pronounced for DYRK1B, with an IC_{50} of 66 nM, whereas for DYRK1A the IC_{50} was 188 nM. These results are consistent with previously reported data, IC_{50}(DYRK1B) = 18 nM, IC_{50}(DYRK1A) = 199 nM and IC_{50}(DYRK1B) = 83 nM, IC_{50}(DYRK1A) = 191 nM in radiometric assay and proximity assay, respectively (*28*). For comparison, using the same assay conditions, IC_{50} values were determined for harmine. Harmine inhibits DYRK1A and DYRK1B with IC_{50} of 97 and 115 nM respectively.

The binding affinities of harmine and AZ191 to DYRK1A and DYRK1B were also evaluated by isothermal titration calorimetry (ITC) (Figure 2D). AZ191 demonstrated a binding affinity of 54 nM to DYRK1A and a stronger binding affinity of 28 nM to DYRK1B, suggesting a slight preference in binding to DYRK1B over DYRK1A. The study also indicated that harmine exhibited a binding affinity of 94 nM to DYRK1A and 29 nM to DYRK1B. This differential binding may reflect potential selectivity, which could be further explored for therapeutic implications, especially in the design of selective inhibitors for DYRK1B.

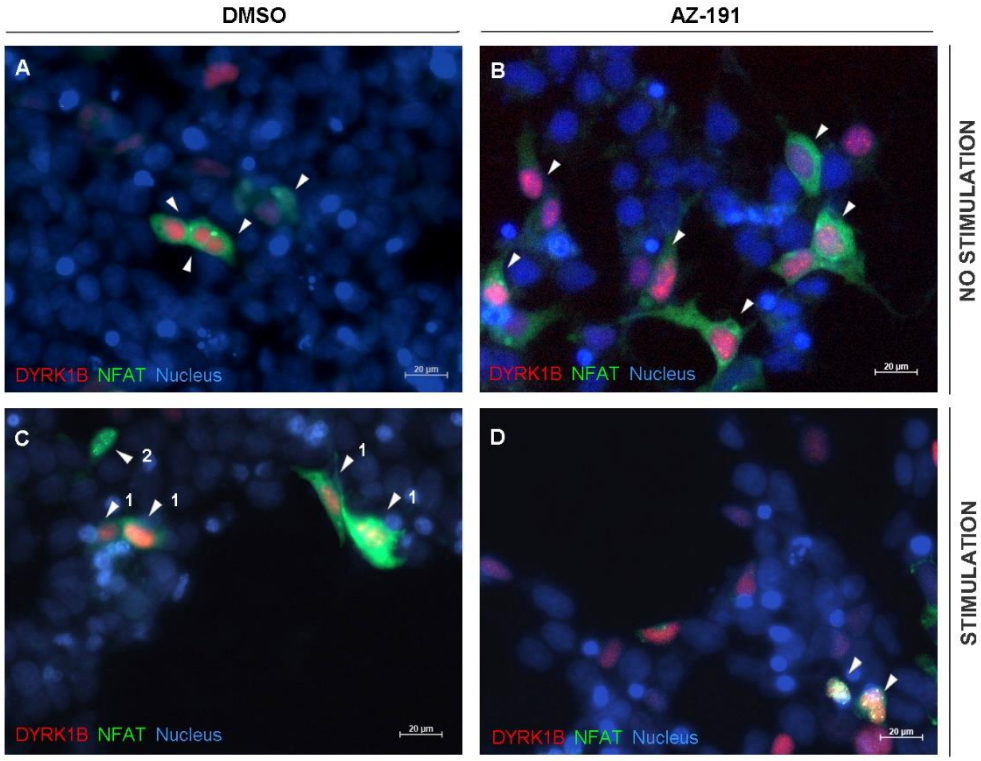

Figure 3. AZ191 treatment restores NFAT signalling by blocking DYRK1B kinase activity. The EGFP–NFATc1 (green) and mCherry-DYRK1B (red) were co-expressed in HEK293T cells. Cells pre-treated for 3 h with AZ191 (10 µM) (B,D) or DMSO (A,C) and stimulated for 1 h with ionomycin (IM; 6 µM) (C,D) or left untreated (A, B). The representative fluorescent images are shown with a scale bar 20 µm.

The high sequence similarity of the kinase domains of DYRK1A and DYRK1B is reflected in an overlapping set of protein substrates. A key pathway affected by both kinases is the NFAT (Nuclear Factor of Activated T Cells) signalling pathway. In this context, DYRK1B-mediated phosphorylation of NFAT impedes its translocation from the cytoplasm to the nucleus, thereby inhibiting subsequent gene transcription. This modulation is significant in various biological contexts, including immune response and neuronal development. Given this background, our study focused on the impact of the DYRK1B inhibitor AZ191 on the calcineurin/NFAT pathway.

We utilized a cellular assay to track the translocation of EGFP–NFATc1 between the cytoplasm and the nucleus. In cells co-expressing mCherry-DYRK1B and EGFP–NFATc1, we observed predominant cytoplasmic localization of EGFP–NFATc1 (Figure 3A). This localization persisted even upon stimulation with ionomycin, a known activator of calcineurin, indicating that mCherry-DYRK1B effectively restrained the nuclear translocation of EGFP-NFATc1 (Figure 3B). However, upon treatment with 10 µM of AZ191, a marked translocation of EGFP–NFATc1 to the nucleus was observed, despite the presence of mCherry-DYRK1B (Figure 3C). This result demonstrates that a concentration of 10 µM AZ191 is sufficient to inhibit DYRK1B activity and thereby restore the functionality of the calcineurin/NFAT pathway in our cellular model.

Crystal structure of DYRK1B in complex with AZ191

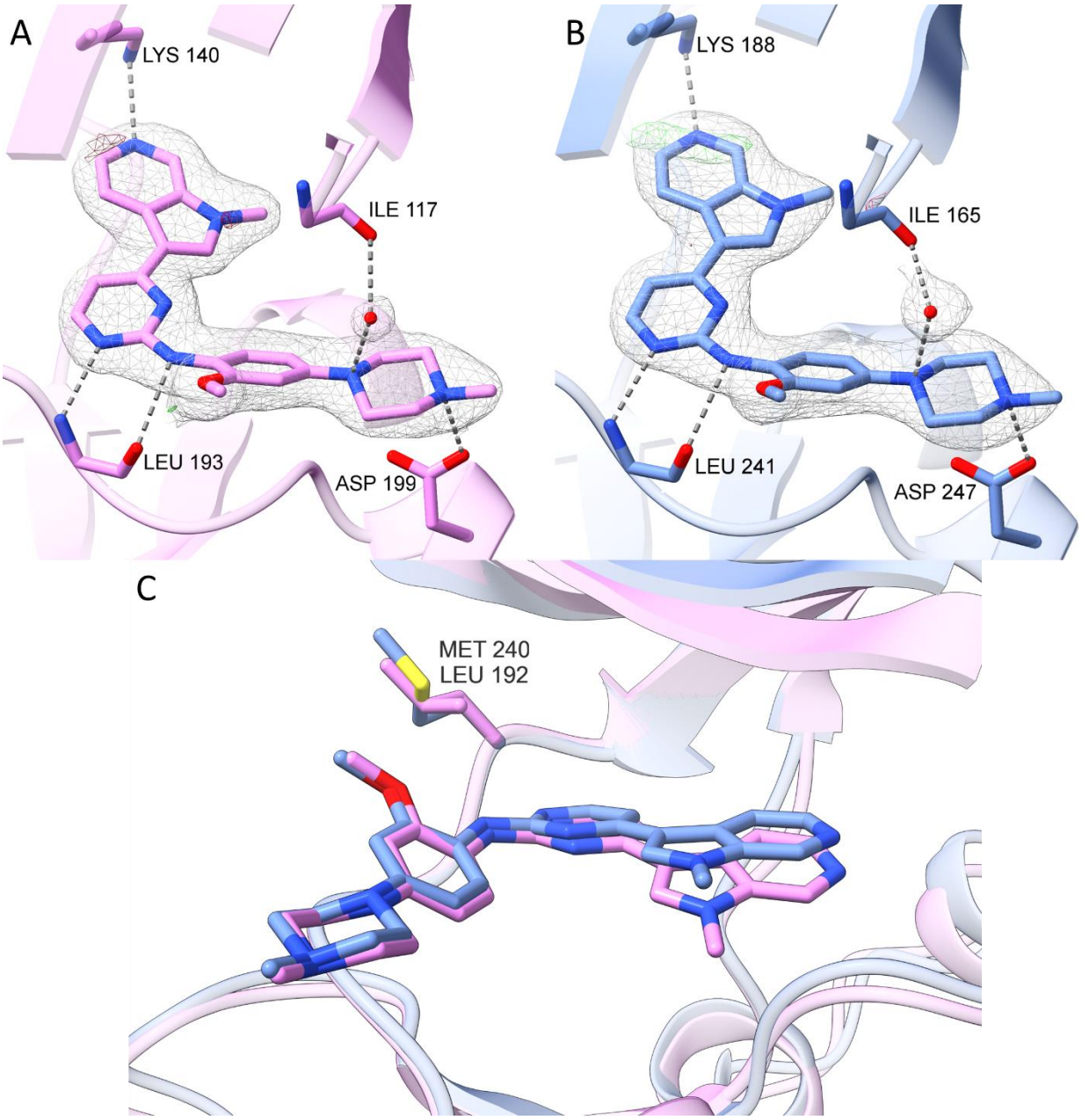

Figure 4. Crystal structures of DYRK1B (pink) and DYRK1A (blue) in complex with AZ191. (A) the binding mode of AZ191 in the ATP-binding pocket of DYRK1B (PDB ID 8C2Z), (B) binding mode of AZ191 in the ATP-binding pocket of DYRK1A (PDB ID 8C3G), (C) superimposition of DYRK1B and DYRK1A ATP-binding pockets with indicated single amino acid difference between their active sites. Hydrogen bonds are shown as dashed lines (dark grey) and the electron density is shown as a mesh, 2Fo-fc: +1.0σ (light grey); Fo-Fc omit map: +3.0σ (green); Fo-Fc omit map: -3.0σ (red).

Alexandrov et al. (*7*) reported a pipeline for optimizing selective inhibitors for DYRK1B. However, the key challenge in this and other structure-based design approaches was the lack of the experimental structure for DYRK1B. Addressing this gap, we successfully expressed, purified, and crystallized the kinase domain of DYRK1B (residues 78 to 442; Uniprot ID Q9Y463) in complex with the inhibitor AZ191 (PDB ID 8C2Z). The kinase crystallized in the $C222_1$ space group,

featuring a single molecule per asymmetric unit. The structure, resolved at a 1.91 Å resolution, delineates most of the molecule clearly, except for portions of the CMGC kinase-specific insert (residues 382 - 394). Furthermore, residues 118 - 124 in the glycine-rich loop, residues 248 - 253, residues 266 - 273 within the activation loop and the regions encompassing additional parts of the CMGC insert (residues 357 - 369, 378 - 381 and 395 - 400) exhibit higher temperature factors compared to the rest of the molecule. This observation suggests that these areas possess structural flexibility, a detail that could be crucial for understanding the kinase's functional dynamics and for the design of more effective inhibitors.

The overall structure of DYRK1B resembles that of protein kinases of the CMGC group, with a bilobal fold and the active site located in a cleft formed between these lobes. The structure exemplifies an active, DFG-in conformation. The smaller, N-terminal lobe is composed mostly of β-sheets and contributes the catalytic lysine (Lys140). The larger C-terminal lobe is composed primarily of α-helices and contributes the activating tyrosine residue within the Y271-x-Y273 motif. A clearly defined electron density represents Tyr273 phosphorylation (Figure S6). Because the kinase was expressed in bacteria, where posttranslational modifications are relatively rare compared to eucaryotes, it is probable that the modification results from autophosphorylation. This is in good agreement with previous findings suggesting that DYRK1B undergoes autophosphorylation (*31*). Overall, the crystal structure of DYRK1B kinase domain determined in this study overlays well with CK2α (PDB ID 3NSZ) and GSK3β (PDB ID 1PYX), the best characterized kinases of the CMGC group. The RMSDs are of 1.16Å for 54.5% of C_α atoms and RMSD of 1.22Å for 57.2% of C_α atoms, for CK2α and GSK3β, demonstrating high structural similarity.

AZ191 exemplifies an ATP mimetic kinase inhibitor and, accordingly, is located at the putative ATP binding site of DYRK1B (Figures 4A and B). The pyrimidine ring contributes a canonical interaction with the backbone amine of Leu193 within the hinge region. The methyl-pyrrolopyridine group penetrates deep into the pocket in the direction of the catalytic Lys140. The discussed moiety is stabilized by a direct hydrogen bond with the sidechain amonium of Lys140, π-stacking interactions with the sidechains of the gatekeeper residues Phe190 and Phe122, and hydrophobic interactions contributed primarily by the sidechains of Val125 and Val258. The methylpiperazine moiety of AZ191 is commonly found in several kinase inhibitors and generally protrudes out of the pocket into the solvent which is also the case in our structure. What is characteristic of AZ191, however, is that methylpyrazine contributes to affinity by providing a hydrogen bond with the sidechain carboxyl of Asp199. Additionally, this methylpyrazine contributes a water mediated hydrogen bond with the mainchain of Ile117. The methoxyphenyl linker contributes a π-lone pair interaction with the backbone carbonyl of Ser194, hydrogen bond with Leu193, and hydrophobic interactions with the sidechain of Ile117. The methoxy substituent stabilizes the rotation of the moiety at the binding site.

Phosphorylation of Tyr273 provides an anchor point for a network of hydrogen bonds stabilizing the position of the sidechain of Tyr273 at the surface of the kinase. These include salt bridges with the guanidine moieties contributed by Arg277 and Arg280. A water mediated hydrogen bond with the sidechain of Ser276 further stabilizes the sidechain of Tyr273 and thereby the orientation of the Leu266-Ser276 linker. This region constitutes the peptide substrate binding site and is unstructured

in related unphosphorylated kinases. Thus, the phosphorylation regulates the activity by stabilizing the substrate binding cleft as has been described earlier for other kinases of the CMGC group.

Crystal structure of DYRK1A in complex with AZ191

DYRK1B and DYRK1A kinases share sequence identity of 85% among the catalytic domain residues. The identity is even higher for residues composing the active site. At such high evolutionary relatedness, the design of selective inhibitors is highly challenging, and success relies on subtle differences at the active site. Several crystal structures of DYRK1A with inhibitors were previously solved and reported. Collectively, this data allows comparison with our structure of DYRK1B in search of anchor points of specificity, but minor differences are best pinpointed in structures with identical inhibitors. Consequently, we determined the structure of the DYRK1A kinase domain (residues 126-489, Uniprot ID Q13627) in complex with AZ191 (PDB ID 8C3G).

The DYRK1A in complex with AZ191 crystalized in the $P2_12_12_1$ space group, and the asymmetric unit comprised of 4 molecules. The crystals diffracted to 2.08 Å resolution. A well-defined electron density documents phosphorylation at the Tyr321 residue (Figure S6 B-E). Accordingly, the structure reflects that of a catalytically competent enzyme. Each kinase molecule in the asymmetric unit contains a clearly interpretable electron density describing the inhibitor (Figure S6 B-E). The protein molecules contained in the asymmetric unit are virtually identical and the inhibitor dispositions at the active site of each molecule contained in the asymmetric unit do not differ. Thus, only model A is considered in further analysis.

The interactions guiding the inhibitor affinity are virtually identical to those observed in DYRK1B (Figure 4A and C). Hydrogen bonds contributed by the sidechains of the catalytic Lys188, Asp247, and the mainchain of Leu241 in the hinge region (equivalent to Lys140, Asp199, and Leu193 of DYRK1B, respectively) anchor AZ191 at the active site of DYRK1A. Further, the methylpyrazine moiety contributes a water mediated hydrogen bond with the mainchain of Ile165 (an equivalent interaction is found with Ile117 in DYRK1B), although the said water is found only in molecules A and C. Further, the inhibitor is stabilized by major hydrophobic interactions contributed by Ile165, Phe170, Val173, Phe238, Leu294, and Val306 (equivalent to Ile117, Phe122, Val125, Phe190, Leu246 and Val258 of DYRK1B, respectively).

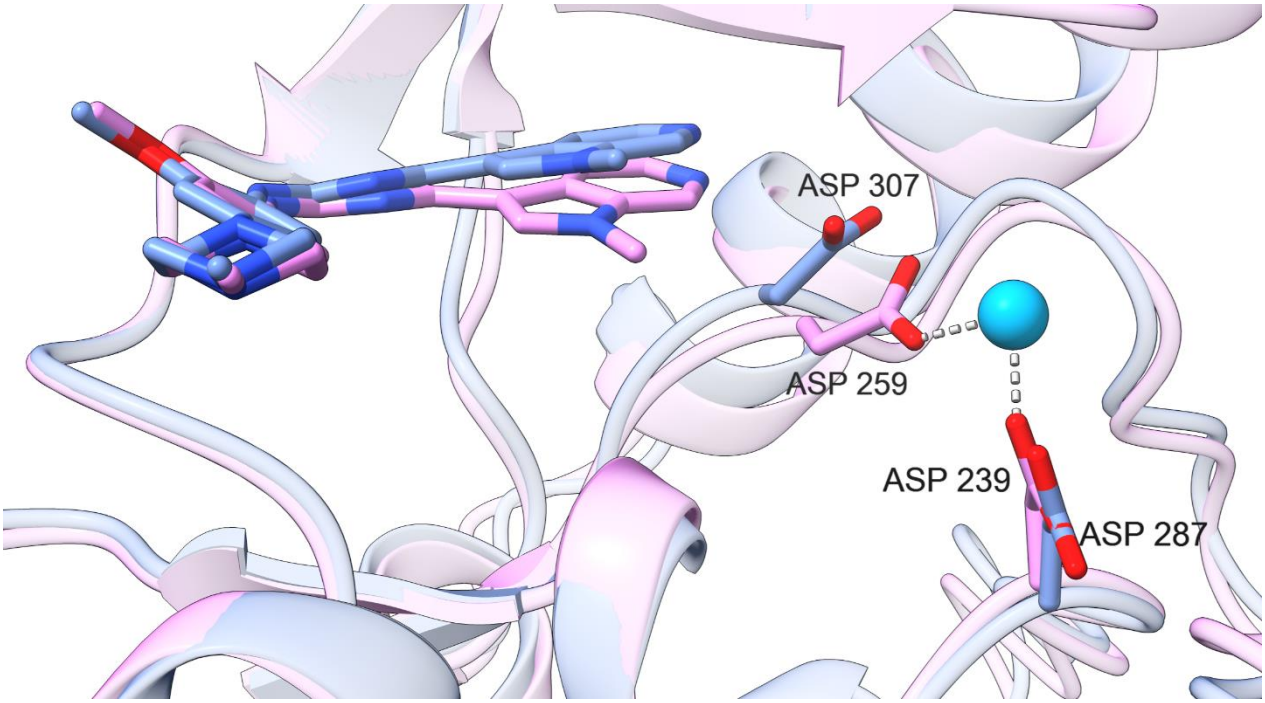

Figure 5. Superimposition of DYRK1B (pink) and DYRK1A (blue) in complex with AZ191 (PDB ID 8C2Z and 8C3G, respectively) with indicated Mn^{2+} ion bound to DYRK1B.

When comparing the AZ191 inhibitor in the co-crystal structure with DYRK1B to that with DYRK1A, different orientations of the methylpyrrolopyridine moiety are observed (Figure 5). In the structure of DYRK1B, the aromatic group is positioned closer to the C-lobe region. The difference, however, is not expected to be related to the fine details distinguishing the kinase active sites, but it rather reflects the different crystallization conditions, which in the case of DYRK1B further contained Mn^{2+} ions. In the DYRK1B structure, the manganese ion coordinates the sidechains of Asp239 and Asp259, reorienting them away from the ATP binding pocket. This affords additional space for methylpyrrolopyridine reorientation when compared to DYRK1A. In the structure with DYRK1A, the absence of manganese ion allows the sidechain of Asp307 (corresponding to the Asp259 in DYRK1B) to displace the methylpyrrolopyridine group of AZ191 towards the N-lobe. Apart from the influence of the ion, the binding modes of AZ191 at the active site of DYRK1B and DYRK1A are virtually identical, reflecting the comparable affinity of the inhibitor to both kinases (Figure 2C).

Despite the overall identity of the binding sites and inhibitor stabilizing interactions, the direct overlay of DYRK1B and DYRK1A crystal structures in complex with AZ191 points to a notable difference in the overall structures of the kinases. The active site of DYRK1B is narrower, compared to that of DYRK1A which is related to the closing of the N- and C-terminal lobes around the hinge region. The N-lobes of DYRK1B (residues 88-190) and DYRK1A (124-238) show a high degree of structural similarity, with RMSD of 0.34 Å for 75.7% of C_α atoms (Figure S5A). The C-lobes (residues 197-434 and 245-490 for DYRK1B and DYRK1A, respectively) also display similar pattern, with RMSD of 0.39 Å for 72.3% of C_α atoms (Figure S5B). However, when comparing the overall structures of the kinase domains, the RMSD is 0.89 Å for 80.5% of Cα atoms. The increase in RMSD value, suggests that the N- and C-lobes are oriented differently relative to each other in the two kinases. To determine whether differences in the relative orientation of the N-

and C-lobes are characteristic of DYRK1B, we compared its structure against all available crystal structures of DYRK1A. From the structural evaluation we concluded that this scissor-like relative relocation of the lobes around the hinge is characteristic of DYRK1A, and our structure with AZ191 reflects one of multiple relative orientations of the lobes. Other structures of DYRK1A present this reorientation of the lobes almost identical to our structure of DYRK1B (*e.g.*, PDB ID 2VX3; RMSD of 0.49 Å for 75.4% of C_α atoms). The apparent relative motions of N- and C- lobes are partly related to crystal packing. The structure of DYRK1A closest to our present one in complex with AZ191 was determined in the same space group (*e.g.*, PDB ID 7FHT; RMSD of 0.30 Å for 89.8% of C_α atoms). On the other hand, the most distal structures with respect to the currently presented structure of DYRK1A with AZ191 were obtained in different space groups. Overlaying our crystal structure of DYRK1B with the most closely related structure of DYRK1A shows overall negligible differences.

Apart from the differences induced by crystal packing and crystallization conditions, the ATP binding pockets of DYRK1B and DYRK1A are virtually identical, safe only for a single residue at the hinge region (Figure 4C). In the structure of DYRK1B, the sidechain of Leu192 is close to the methoxy group in the inhibitor, though it does not contribute with significant interactions. The equivalent residue in DYRK1A, Met240, has a slightly longer sidechain, which comes closer to the inhibitor. Convenient exploration and optimization of these interactions by modifications of substituents at the phenyl ring of AZ191 should allow tackling the specificity of this class of inhibitors. Other scaffolds could also explore this pocket to achieve selectivity.

Quantum Mechanical Analysis of Binding

Despite overall structural similarity and an almost exact identity in the binding pocket, DYRK1A and DYRK1B show different binding affinities ($\Delta G = RT \log[Kd]$) and selectivities towards inhibitors. In particular, the binding affinities towards AZ191 differ by a factor of two ($\Delta\Delta G \sim 0.41$ kcal/mol). Differences in other thermodynamic data are more pronounced, like enthalpies of binding, indicating that there are subtle differences between the two kinases that could be explored for selectivity. To better understand the underlying mechanisms behind such fine selectivity, we decided to employ our Energy Decomposition and Deconvolutional Analysis algorithm (EDDA) (*33*). EDDA is a quantum mechanical-based algorithm that partitions interaction energies into different contributions, namely electrostatics, polarization, dispersion (lipophilicity), repulsion (shape complementarity), solvation, and charge transfer. This partition allows the determination of the nature of protein-ligand interactions, allowing the quantification of the main forces that lead to binding. Specifically, electrostatics measures the interaction of atoms of different molecules as point charges. Polarization measures the adaption of the electronic density of the ligand due to the presence of the protein. This corresponds to an intramolecular flow of electrons. Charge transfer describes an intermolecular flow of electrons (when the ligand shares part of its electron density with the protein). These two types of interactions, polarization and charge transfer, affect both interaction partners, meaning that additional contributions arise from the impact of the ligand onto the protein. As negative-charged species, electrons will tend to avoid regions in space overcrowded by other electrons. This brings about a correlation in electronic motion that generates instantaneous fluctuations in the electronic densities. These interactions give rise to dispersion interactions, which account for a stabilizing effect in lipophilic contacts. Since molecules have volume (electronic density), whenever these interact there will be regions in space where electronic densities clash.

This overlap of electronic densities generates a repulsive force between the molecules which is accounted for by the repulsion term. Lastly, protein-ligand complexes are formed in an aqueous solution. The solvent will stabilize differently the molecules involved in binding, potentially (dis)favouring the binding event. To better understand the locality of protein-ligand interactions, all interaction components are partitioned in pairwise contributions, which allow us to build interaction maps. These allow us to evaluate the key contributors that lead to the formation of the bound complex in each protein. Overall, a different understanding of fine differences in protein-ligand interactions is achieved that can hint at which elements can be used to exploit kinase selectivity. Figure 6 collects the electrostatics, dispersion (lipophilicity), repulsion, and total interaction maps for the inhibitor AZ191 in each kinase. Figure 6 also contains a column plot of decomposed energies. Additional maps and the respective calculated values are given in supplemental information (Figures S7-S9 and Table S2).

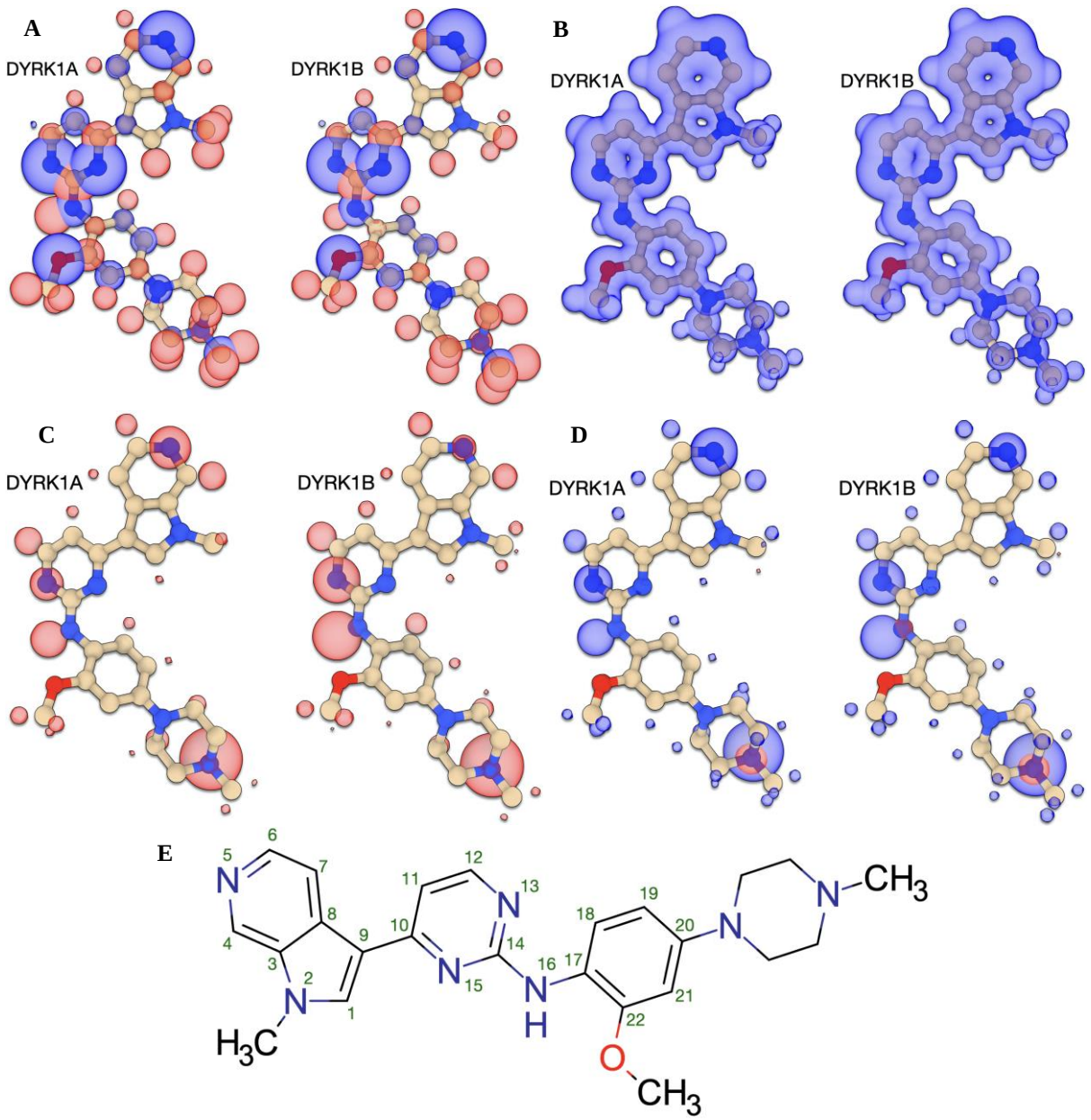

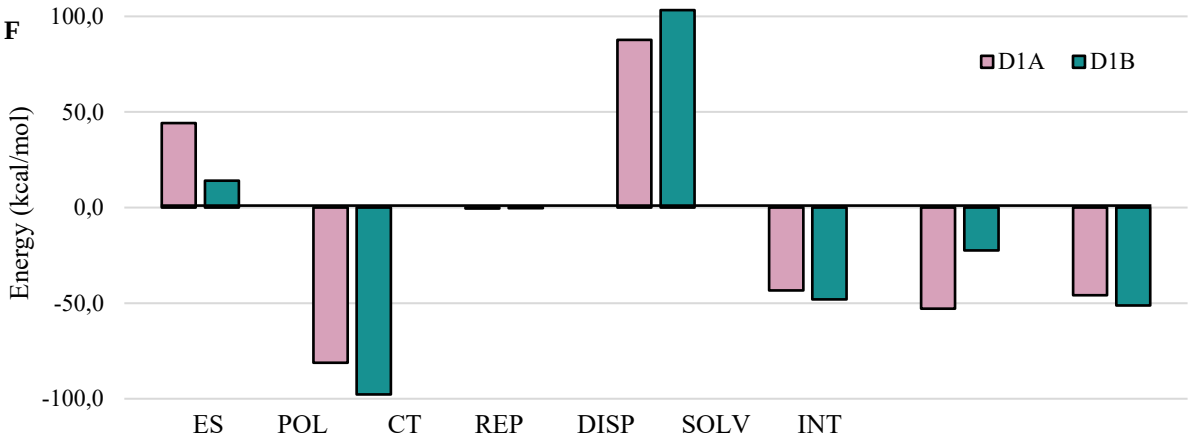

Figure 6. The decomposition analysis of the binding energy of AZ191 in DYRK1A and DYRK1B. (A) The electrostatics (ES), (B) dispersion (DISP), (C) repulsion (REP), and (D) total interaction imaps for AZ191 in the kinases. (E) The structure of the ligand and the atomic numbering used in the discussion. (F) Decomposed energies.

The immediate observation when analysing the imaps for AZ191 in each kinase is that the landscape of interactions is virtually indiscernible between the two DYRKs analysed (Figure 6 A-D). This reflects the sequence homology around the ATP binding pocket. The main foci of interactions are N5, binding to the catalytic lysine; the hinge binding at N15 and N16; the external nitrogen from the piperazine moiety. The total interaction maps (Figure 6D), despite their similarity, reveal that the ligand binds stronger to the hinge of DYRK1B than to DYRK1A. The total interaction energies, comparable to enthalpies of binding, differ by 5.4 kcal/mol (in favour of DYRK1B), which is remarkably close to the 5.0 kcal/mol measured by ITC. This establishes a strong parallel between our experimental and computational data. The electrostatics maps (Figure 6A) show more bipolar interactions in the case of DYRK1A, which, when coupled with the repulsion and charge transfer imaps indicate a smaller covalent character for the hydrogen bonds in this kinase. It is particularly interesting in the case of the linker N16, where the differences in imaps are clearer. Interestingly, the distance between N15 and N16 to the hinge binding atoms is shorter in the case of DYRK1B, by almost 0.2 Å (each bond). Repulsion maps (Figure 6C), which measure the overlap of electronic densities of the two molecules in certain domains of interaction, indicate a stronger contact in the case of DYRK1B. This evidences that the higher covalent character in the hydrogen bonds between AZ191 and the hinge atoms of each DYRK1 kinase is primarily an effect of how close the respective atoms are, and not so strongly on the overall charge distribution of each protein.

The interaction of N5 with the catalytic lysine is weaker in the case of DYRK1B. Though not apparent from the viewpoint of electrostatics, it is so from the repulsion and total interaction maps. Again, the effect seems to be primarily distance-related, as the respective hydrogen bond is shorter by almost 0.4 Å in the case of DYRK1A. This identifies a subtle difference in the binding poses of AZ191 in each kinase. Lastly, the interactions between the piperazine group and the proteins are identical.

To understand whether the different interactions with the hinge and the catalytic lysine are meaningful from the binding viewpoint, or whether these result from crystal artifacts (e.g., lacking the dynamics of the protein-ligand complex), we took a closer look at the total repulsion energy for

each complex. Overall, this value is larger in DYRK1B by over 15 kcal/mol (Figure 6F), which indicates a stronger overlap of the electronic densities of protein and ligand. This very same difference can also be followed in the respective maps (Figure 6C), which show overall more intense contacts between DYRK1B and the ligand. The only exception is N5, the atom responsible for tackling the catalytic lysine. Here, the interaction is more pronounced for DYRK1A, which is followed in all maps. Coupled with the total interaction maps, electronic repulsion indicates a clear difference in the interaction modes, which were already discussed: the ligand AZ191 captures more effectively DYRK1B by the hinge, whereas in DYRK1A the interactions with the hinge and the catalytic lysine are more balanced. Indirectly, this hints that the accessibility of the catalytic lysine of DYRK1B is lower, which seems to constitute a convenient element to exploit selectivity.

The Dynamics of DYRK1A and DYRK1B

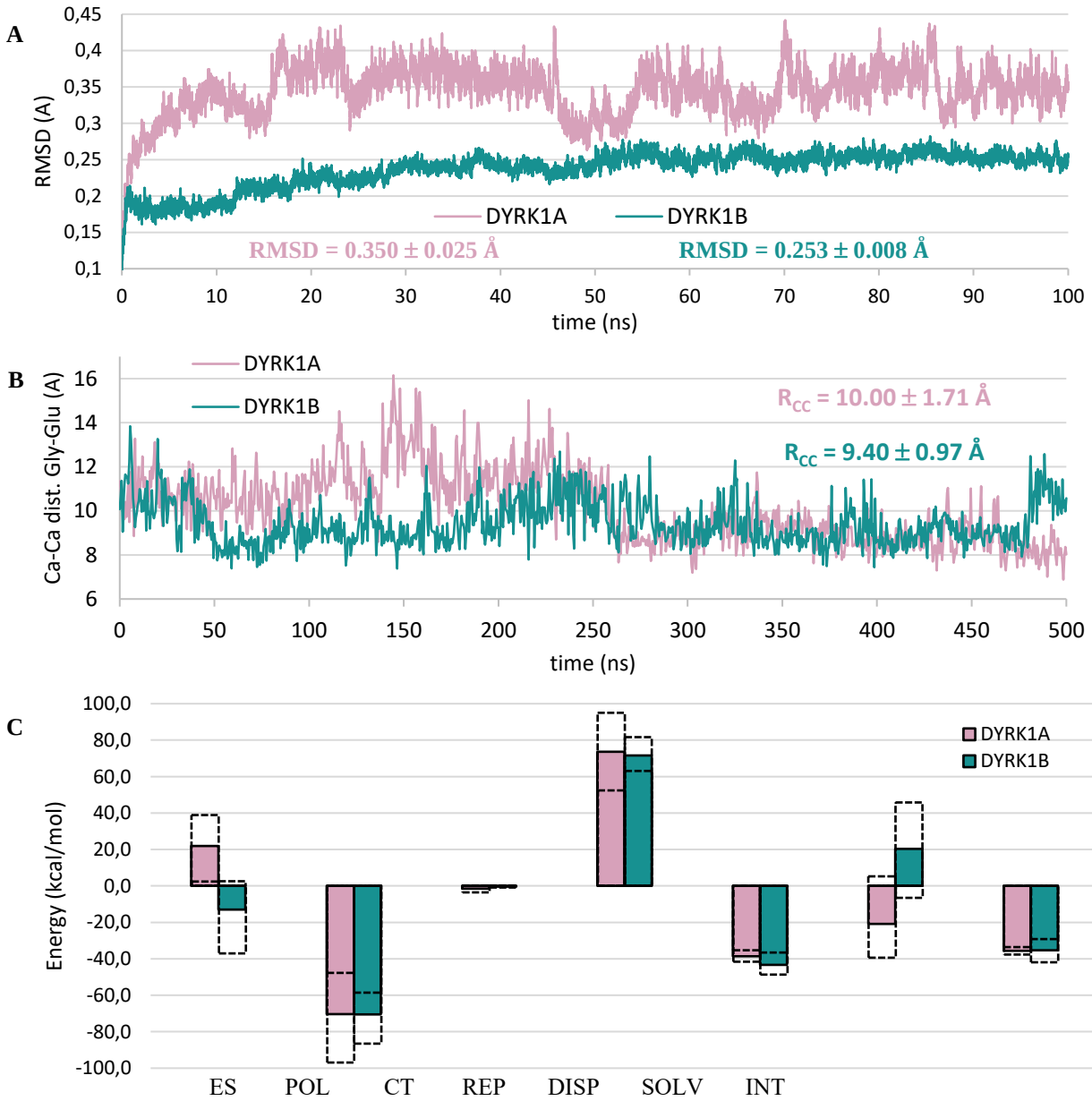

Figure 7. The dynamics of the apo and AZ191 bound DYRKs. (A) RMSD of pocket residues as a function of time. Average RMSDs and the respective standard deviations that are given in the plot were obtained for the last 40 ns of simulation time. (B) The distance between the Cα in the Gly-Glu residues of each DYRK (for DYRK1A: Gly168-Glu291; for DYRK1B: Gly120-Glu243) as a function of time. Average distance (and standard deviation) calculated after the first 100 ns of simulation time. (C) Time-averaged EDDA on DYRK1A and DYRK1B with AZ191 and the respective limits observed for each contribution. EDDA conducted on the larger subsystem B.

To better understand the behaviour of DYRK1A and DYRK1B, apo and with inhibitor, a series of molecular dynamics (MD) simulations were conducted. MD and EDDA results on the MD traces are presented in Figure 7 (see supplemental Tables S3-S6 for additional data).

The most immediate remark from the simulations on apoproteins is that DYRK1A shows larger flexibility than DYRK1B. This is reflected in the RMSD data from the dynamical traces (Figure 7A). On average, DYRK1A also shows larger distances between residues on the N- and C-lobes, with wider amplitude movements (Figure 7B). This is, however, an artifact of the simulation, as it took longer for DYRK1A to relax from the starting structure with the ligand's imprint. After about 250 ns, DYRK1A closes the pocket, remaining in this state until the end of the simulation. This we identify as the resting state of the kinase, which is identical for both paralogs (Figure S11).

Figure 7C shows time-averaged EDDA results on both protein-ligand complexes. It is interesting to observe that all interactions decrease in magnitude compared to the crystal structure calculations. Most contradictory, the average shape complementarity emerges now larger in DYRK1A. The average binding energy also favours DYRK1A, which is a mismatch with experimental data. Though DYRK1B shows larger variations in binding energy that could be used to argue in favour of the simulation, the EDDA binding energy as a function of time decreases for DYRK1A and increases for DYRK1B. These clear trends, together with simulation snapshots, indicate the inability of AZ191 to reach DYRK1B's catalytic lysine in comparison to DYRK1A. This is reflected in the distances between the ligand's N5 and the NZ of the catalytic lysine (Figure S12): on average, as obtained from simulation, 3.17 Å for DYRK1A and 3.51 Å for DYRK1B; the latter are in marked contrast with the experimental values of 2.92 and 2.97 Å for the same kinases. Though this imbalance surely warrants caution when analysing MD results, we believe this behaviour from the force field further stresses the differences pointed out previously on the accessibility of the catalytic lysine. This naturally raises the question: how is it possible for two kinases that show such remarkable sequence and structural similarities to exhibit such disparate behaviour on their ATP-binding pockets, which allows biological systems to exploit selective kinase activity? Answer to this question, the long-range effect of distal residues, is corroborated by calculations (Table S7): as the number of protein atoms included in calculations increases, electrostatics become less repulsive. The impact of distal residues extends, however, to other interactions. The repulsion energy between the inhibitor and the protein increases with the pocket size. By including larger protein domains in the calculations, fine changes in the charge distribution and electronic populations take place, which affect how the two molecules interact. Note that because of the exponential decay of repulsion with distance, the 9 kcal/mol difference in repulsion implies only punctual modifications in the electronic densities. Overall, the calculations provide a

clear atomic mechanism underlying selectivity between the two kinases, which could only be uncovered by including electronic effects in the calculations.

Discussion

DYRK1A's involvement in neurological disorders, cancer, and diabetes has been well-documented, with significant progress made in inhibitor design and development. However, the translation of these developments into clinical applications remains elusive. In contrast, DYRK1B has only recently been recognized as a potential target in cancer, metabolic syndrome, and non-alcoholic fatty liver disease. The challenge in targeting DYRK1B lies in the poor selectivity of existing probes against related CMGC group kinases and the near absence of selectivity among DYRK inhibitors. While some researchers advocate for selective inhibition of DYRK kinases to mitigate toxicity, concrete evidence supporting this claim is limited. Currently available DYRK1A/1B inhibitors also affect Homeodomain-Interacting Protein Kinases (HIPKs), which are crucial in *Drosophila melanogaster* for eye and wing formation as well as the development of the nervous system and muscles (*34, 35*). The implications of HIPK inhibition in mammals are yet to be fully understood, but the findings in Drosophila suggest the need for thorough testing.

In addition to cross reactivities delineated in previous paragraph, existing DYRK1A/1B inhibitors target Cdc-like kinases (CLKs), with CLK1 involved in cell cycle control-related alternative splicing and CLK2 disruptions leading to widespread cell cycle defects and proliferation loss (*36, 37*). These observations necessitate careful monitoring of the long-term effects of cross-reactive DYRK1A/1B inhibitors. Selective inhibition of DYRK kinases over related CMGC kinases might offer higher efficacy and will be instrumental in defining substrates and downstream effects regulated by these kinases, rather than merely reducing toxicity.

Selective targeting of specific DYRK kinases could be advantageous. DYRK1B activity is implicated in certain cancers and non-alcoholic fatty liver disease, with a gain-of-function mutation in the DYRK1B gene observed in metabolic syndrome. DYRK1B upregulation in ovarian, pancreatic, and non-small cell lung cancers, and its inhibition in certain ovarian cancer cell lines, leads to increased ROS levels and apoptosis, while similar treatment in colon cancer cells expressing only DYRK1A showed no effect (*30*). Elevated DYRK1B levels in non-alcoholic steatohepatitis (NASH) patients correlate with hypertriglyceridemia, fatty liver, and hepatic insulin resistance (*38*). In metabolic syndrome, the R102C gain-of-function mutation in DYRK1B enhances adipogenesis and induces glucose-6-phosphatase expression, a key gluconeogenic enzyme (*17*). However, concurrent inhibition of DYRK1A is not desirable due to the risk of elevated homocysteine levels, as demonstrated in mice (*39*). Where DYRK1A inhibition led to increased circulating homocysteine levels, known for their neurotoxic effects (*40*). These findings underscore the need for *in vivo* testing of the benefits of selective DYRK kinase inhibition.

The development of selective inhibitors differentiating DYRK kinases has been hampered by the lack of an experimental DYRK1B structure. While powerful homology modelling methods exist, the close evolutionary relationship between DYRK1A and DYRK1B means that active site differences are subtle, making initial modelling efforts only approximate. Despite growing interest, DYRK1B eluded structural characterization until now due to challenges in efficient heterologous

expression and the belief that the kinase's flexibility might prevent crystallization. However, these assumptions often reflect temporary experimental difficulties rather than permanent barriers.

Our systematic approach has enabled the development of a reliable expression and crystallization method for DYRK1B. Our structural characterization of DYRK1B, alongside the earlier DYRK1A structures, sets the stage for the rational design of inhibition module. The enzyme-inhibitor interactions follow Koshland's induced fit model (*41*). Thus to minimize the influence of inhibitor variability in our comparative analysis, we also determined the structure of DYRK1A in complex with the same inhibitor, AZ191. Following the high sequence homology, the ATP pockets of DYRK1A and DYRK1B are almost identical, with only a single residue differentiating the two. This site, addressed by the methoxy moiety of AZ191, suggests a convenient mechanism for enhancing specificity. Bulkier substituents are expected to cause a steric clash in DYRK1A due to the ramification in the leucine sidechain, a hypothesis that remains to be experimentally verified. Thus, optimizing interactions at the Leu/Met site appears to be one of the rational approaches for enhancing the selectivity of small molecule ATP mimetic inhibitors based on AZ191 or other scaffolds. The quantum mechanical calculations revealed two additional factors that could be investigated to explore selectivity. Firstly, the ATP-binding pocket's electrostatic environment, influenced by distal residues, differs significantly between the kinases. However, leveraging electrostatics for selectivity is complex due to environmental factors like salt concentrations, which vary between *in vitro* and *in vivo* conditions. Secondly, simulations showed reduced accessibility to the catalytic lysine in DYRK1B, defined by a narrower ATP-binding pocket. This suggests a more stable and environment-independent approach for inhibitor design. Our model hypothesises that DYRK1B's restricted access to the catalytic lysine renders binding to this kinase less sensitive to the bulkiness of the lysine-binding groups. On the other hand, binding to DYRK1A should favour smaller and more compact lysing binding groups. To test this, we examined published data on ligands structurally similar to AZ191, such as Abemaciclib and Cirtuvivint (*28*). The interaction with the catalytic lysine is key to both the inhibitors and involves a benzimidazole ring in Abemaciclib and a pyrazole ring in Cirtuvivint. Abemaciclib, which contains a bulky isopropyl group in its benzimidazole ring, shows a 5-fold higher affinity for DYRK1B than DYRK1A. Conversely, Cirtuvivint, with a smaller methyl group near the compact pyrazole ring, exhibits a 5-fold lower affinity for DYRK1B than DYRK1A. Additional evidence comes from ARN25067 and TCMDC-135051 (*28*). both with bulky substituents near the lysine-binding groups, resulting in a preference for DYRK1B (factor of 8 for ARN25067 and factor of 2 for TCMDC-135051). Similarly, compounds SM77 and SM330 (*28*) lacking bulky substituents, bind more strongly to DYRK1A (factor of 2-3). EHT-1610, with its non-bulky methyl acetimidate group, also shows stronger binding to DYRK1A by a factor of 3. Our model also explains the slight preference of AZ191 for DYRK1B, given its indole ring's size in capturing the catalytic lysine.

In conclusion, our crystal structure of DYRK1B kinase opens the door for the development of selective inhibitors. The almost identical ATP pockets of DYRK1A and DYRK1B underscore the challenge of this endeavour, but the Leu/Met site and the accessibility of the catalytic lysin offer potential anchor points. Future development of selective inhibitors will enable the assessment of whether selective targeting is indeed more beneficial than current inhibitors that target both kinases with similar potency.

Materials and Methods

Plasmid construction

The gene encoding the kinase domain of DYRK1B (78-442; Uniprot ID Q13627) was codon optimized, synthesized by Genscript and cloned into a pET24a plasmid. The kinase domain of DYRK1B was expressed with a C-terminal tobacco etch virus (TEV) protease cleavage site followed by His-Tag (ENLYFQ*GHHHHHH).

The gene fragment encoding the kinase domain of DYRK1A (126-490; Uniprot ID Q9Y463) was PCR amplified from plasmid pEXP17-DYRK1A (*42*) and subcloned into pET24a plasmid. The kinase domain of DYRK1A was expressed along with a non-cleavable C-terminal His-Tag.

Protein expression and purification

DYRK1B was expressed in *E. coli* LOBSTR strain (Kerafast) in TB medium supplemented with kanamycin (50 µg/mL) at 17 °C. 16 hours after the induction the cells were harvested by centrifugation and the pellet was resuspended in lysis buffer (20 mM HEPES pH 7.5, 300 mM NaCl, 5% glycerol, 15 mM imidazole, 5 mM $MgCl_2$, and 5 mM 2-mercaptoethanol) and lysed by sonication. Clarified lysate was incubated with HisPur™ Cobalt resin (ThermoFisher Scientific, Waltham, MA, United States) for 1 hour at 4 °C, and DYRK1B was eluted with increments of imidazole concentration (50–300 mM). The elution fractions were pulled and dialyzed against 20 mM HEPES pH 7.5 containing 150 mM NaCl, 5mM $MgCl_2$, 5 mM 2-mercaptoethanol and TEV protease. Released His-tag was removed by reverse chromatography on HisPur™ Cobalt resin. Final purification was obtained on HiLoad 16/600 Superdex 75 pg column (Cytiva) in 20 mM HEPES pH 7.5 containing 150 mM NaCl, 5 mM $MgCl_2$ and 1 mM TCEP.

The expression and initial purification steps for DYRK1A were identical to DYRK1B. Following cobalt affinity chromatography, the kinase was dialysed into 20 mM HEPES pH 7.5 containing 50 mM NaCl, 5 mM $MgCl_2$ and 5 mM 2-mercaptoethanol. Further purification was obtained by ion-exchange chromatography on HiTrap Q FF column (Cytiva) followed by size exclusion chromatography as for DYRK1B.

Purified proteins were flash-frozen in liquid nitrogen and stored at −80 °C for further analysis.

Dye-based Thermal Shift Assay

DYRK1A and DYRK1B kinase domain stability in the presence of harmine and AZ191 were analysed by the proteins' melting temperatures determination using Thermal Shift Assay (TSA) as described previously (*43*). Both proteins (1.5 mg/ml) were incubated with 1:200 diluted Sypro Orange dye 20 mM HEPES pH 8.0, 100 mM KCl, 10 mM $MgCl_2$, 1 mM 2-Mercaptoethanol and compound (10 µM) or DMSO. The fluorescence signal of Sypro Orange was determined as a function of temperature between 5 and 95 °C in increments of 0.5 °C min^{-1} (λ_{ex} 492 nm, λ_{em} 610 nm). The melting temperature was calculated as the inflection point of the fluorescence as a function of temperature. The experiment was carried out in triplicates.

Cellular Thermal Shift Assay (CETSA)

The interaction between AZ191 and full-length DYRK1B kinase was analyzed by cellular thermal shift assay in complex cell lysate. Samples were prepared from control and inhibitor-exposed cell lysates. For each set, 2×10^7 cells were seeded in a 10-cm cultured dish. After 24 h of culturing, the cells were transfected with plasmid encoding Flag-DYRK1B using PEI Prime (Sigma-Aldrich), then 4 h later medium was changed and cells were left for 48 h. Then cells were treated with AZ191 (10 µM) or DMSO. 24 h later the cells were washed with PBS, treated with trypsin and collected by centrifugation at 1200 rpm for 5 min at room temperature. The pellets were gently resuspended in 800 µl of RIPA lysis buffer (Sigma-Aldrich) supplemented with Protease Inhibitor Cocktail (Roche) and disintegrated by sonication. The samples were centrifuged at 20 000 rpm for 30 min at 4 °C, and the supernatants were transferred to new Eppendorf tubes. Pairs consisting of one control aliquot and one experimental aliquot were heated at 40 °C, 45 °C, 50 °C, 55 °C, 60 °C, 65 °C or 70 °C for 5 min. Next the samples were cooled on ice, centrifuged at 20 000 rpm for 30 min at 4 °C and supernatants were analyzed by Western Blot using monoclonal ANTI-FLAG M2-Peroxidase (HRP) antibody (Sigma-Aldrich, A8592).

ADP-Glo kinase activity assay

The inhibitory potency (IC_{50}) of harmine and AZ191 was determined with the ADP-Glo kinase activity assay (Promega). The synthetic peptide DYRKtide (RRRFRPASPLRGPPK, Caslo ApS) was used as a substrate for DYRK1A and DYRK1B. 20 µl of kinase in reaction buffer (100 mM MOPS pH 6.8, 100 mM KCl, 10 mM $MgCl_2$) and 10 µl of compound were incubated for 15 minutes at room temperature. The reaction was started by simultaneous addition of 20 µl of substrates mix (ATP and DYRKtide) and continued for 30 minutes at room temperature. The 5 µl of reaction mixture was transformed to HTRF 96 well low volume plates (Cisbio) and the consumption of ATP was measured with ADP-Glo Kinase Assay kit (Promega Corporation) according to manufacturer protocol. The final composition of reaction reagents was - kinase (DYRK1A, DYRK1B) 5 ng/µl, compound (harmine, AZ191) 5 nM – 5 µM, ATP 100 µM and DYRKtide 400 µM. All measurements were done in triplicate and IC_{50} was determined using GraphPad Prism software.

Isothermal titration calorimetry measurements

ITC was performed with Nano ITC 2G (TA Instruments). To measure the DYRK1A interaction with harmine and AZ191, the proteins were dialyzed overnight at 4 °C against the ITC buffer (20 mM HEPES, 150 mM NaCl, 1 mM TCEP and 0.2% DMSO) . The reaction cell was filled with a respective protein solution (10 µM) whereas harmine or AZ191 was prepared in the same ITC buffer at 100 µM (from 50 mM stock solution) and loaded into a dosing syringe. All samples were degassed using an accessory degassing system (TA Instruments) prior to being placed in the ITC to minimize the possibility of gas bubble formation during the run by pulling a vacuum of 0.3–0.5 atm for 10–15 min. Each injection (5 µl) was performed in 300 s intervals. All experiments were conducted at 25 °C with a stirring rate of 250 rpm. The results were analyzed using NanoAnalyze software (TA instruments).

NFAT translocation assay

HEK293T cells were grown on μ-Slide 8 well (IBIDI) to 50%–70% confluency. The plasmids expressing mCherry-DYRK1B and eGFP-NFATc1 were transiently co-transfected for 48 h with PEI Prime (Sigma-Aldrich). Cells were pre-treated with inhibitor AZ191 (10 μM) or DMSO for 3 h and then stimulated with ionomycin (Thermo Fisher Scientific) for 1 h. Cells were washed with 1 ml PBS and the nuclei were stained with Hoechst 33258 (ThermoScientific) for 10 min at 37 °C and fixed with 4% paraformaldehyde in phosphate-buffered saline (PBS) for 10 min at 25 °C. Images were collected with Zeiss Axio Observer 3 fluorescence microscope and analysed in ZEN Blue edition software.

Mass Spectrometry

Samples for MS were taken during first step of protein purification (after sonication) and final purified protein. Bottom-up protein identification with phospho-modified residues was done according to the typically used protocols. Briefly, sample in the form of Coomassie Brillant Blue stained band was excised and destained (ammonia-bicarbonate/AMBIC buffer 50 mM, pH=8.0/acetonitrile). Then the band was rehydrated in the AMBIC buffer with following routine reduction (5 mM DTT, 10 min, 80°C, with shaking) and cysteine alkylation (5 mM iodoacetamide, 10 min, 80°C, with shaking) procedure. Peptides were eluted from the gel, using water/acetonitrile/formic acid mixture (9/10/1 v/v/v), then freeze-dried and dissolved in the 60 μl of 4% acetontrile/water solution supplemented with 0.1% formic acid. 5 μl were introduced into the nanoLC-MS/MS system. Equipment used: nanoLC: Ultimate 3000 (Thermo, Bremen, Germany) in the set-up containing trap cartridge (Acclaim Pepmap 100, C18, 1 mm ID, 5 mm length, particle size 5 μm) and analytical column (Acclaim Pepmap 100, C18, 75 μm ID, 150 mm length, particle size 3 μm). Mass spectrometer: Exploris 240 (Thermo, Bremen, Germany) equipped with Nanopray FLEX ion source. Peptides separation was done using following solvents: A: water+0.1% formic acid, B: acetonitrile + 0.1% formic acid. Gradient settings: T=0 min 5%B, T=5 min 5%B, T=20 min 35%B, T=22 min 75%B, T=23 min 75%B, T=25 min 5%B, T=30 min 5%B. Mass spectrometer settings: MS spectrum range: 350-1600 m/z, resolution 30000, MS/MS spectrum range: 200-2000 m/z, resolution 60000. Up to 6 fragmentation scans between MS scans. Ion exclusion for 20 sec after 2 MS/MS scans.

Data analysis was done as follows: conversion from raw to mgf files was done with the aid of RawConverter software, ver. 1.1.0.23 64-bit (from: http://fields.scripps.edu/rawconv/). Mgf files were searched against the database containing the single sequence of the protein-of-interest (DYR1B_HUMAN). Search engine was the local Mascot server, ver. 2.8.0 (Matrixscience, UK). Mascot settings were as follows: enzyme: trypsin, up to 2 missed cleavages; fixed modifications: carbamidomethylation; variable modifications: Met-oxidation, phospho (ST), phospho (Y); MS and MS/MS tolerances: 100 ppm; #13C = 1; peptide charge: 2+, 3+ and 4+; instrument: ESI-FTICR.

Protein crystallization, data collection and structure determination

DYRK1B was concentrated to 10-13 mg/ml and incubated overnight with 5-molar excess of AZ191 at 4 °C. For crystallization condition screening the preparation was mixed 1:1 (v/v) with

crystallization solutions. The experiments were carried out at 20 °C and crystals appeared within 1-3 days. The best crystals were obtained using sitting drop vapor diffusion setup in 0.1 M Bis-Tris pH 5.5 containing 25% PEG 3350, 0.2 M magnesium chloride and 0.1 M manganese chloride. Crystals of DYRK1A in complex with AZ191 were obtained in a manner similar to those of DYRK1B, but from 0.1 M HEPES pH 7.5 containing 10% PEG 8000, 8% ethylene glycol and 0.1 M ammonium sulfate. Crystals were cryoprotected in mother liquor containing 25% ethylene glycol and flash-frozen in liquid nitrogen.

X-ray diffraction data were collected at BESSY (Berlin) and DESY (Hamburg). The diffraction data was indexed and integrated using XDS (*44*). Data was scaled in AIMLESS (*45*) from the CCP4 software package (*46*). Following steps were performed in Phenix (*47*). The structures of DYRK1B and DYRK1A were solved by molecular replacement using PHASER (*48*) and respective search models: processed AlphaFold model AF-Q9Y463-F1 and PDB ID 7A4O. Models were refined by interchanging cycles of automated refinement using phenix.refine (*49*) and manual building in Coot (*50*). Restraints for the inhibitor were created in Grade Web Server (*51*).

Computational Methods

Energy Decomposition and Deconvolutional Analysis (EDDA) calculations were performed using our in-house quantum chemical package, ULYSSES (*52*). Details of the EDDA method were published earlier (*33, 53*). The quantum chemical method of choice was GFN2-xTB (*54*) with ALPB aqueous solvation (*55*). Molecular Dynamics simulations were conducted using GROMACS (*56*) with OPLS (*57–59*) and CHARMM36 (*60*) force fields. Explicit water was simulated using the TIP3P model (*61, 62*). Simulations were conducted following standard protocols (*63*) in the NPT ensemble. Temperature and density were controlled over all stages to ensure stability of the simulations. Apo protein simulations were run for 500 ns, whereas kinase and ligand systems were simulated for 100 ns. Preparation of the protein for EDDA calculations was done using Chimera (*64*).

Figures

Figures were prepared in ChimeraX (ver. 1.7) (*65, 66*), IBS 2.0 (*67*) and GIMP (ver. 2.10.36).

References

1. L. J. Wilson, A. Linley, D. E. Hammond, F. E. Hood, J. M. Coulson, D. J. MacEwan, S. J. Ross, J. R. Slupsky, P. D. Smith, P. A. Eyers, I. A. Prior, New Perspectives, opportunities, and challenges in exploring the human protein kinome. *Cancer Res* **78**, 15–29 (2018).
2. G. Manning, D. B. Whyte, R. Martinez, T. Hunter, S. Sudarsanam, The protein kinase complement of the human genome. *Science (1979)* **298**, 1912–1934 (2002).
3. M. M. Attwood, D. Fabbro, A. V. Sokolov, S. Knapp, H. B. Schiöth, Trends in kinase drug discovery: targets, indications and inhibitor design. *Nature Reviews Drug Discovery 2021 20:11* **20**, 839–861 (2021).
4. S. Aranda, A. Laguna, S. de la Luna, DYRK family of protein kinases: evolutionary relationships, biochemical properties, and functional roles. *The FASEB Journal* **25**, 449–462 (2011).
5. H. Kentrup, W. Becker, J. Heukelbach, A. Wilmes, A. Schürmann, C. Huppertz, H. Kainulainen, H. G. Joost, Dyrk, a dual specificity protein kinase with unique structural features whose activity is dependent on tyrosine residues between subdomains VII and VIII. *Journal of Biological Chemistry* **271**, 3488–3495 (1996).
6. W. Becker, H. G. Joost, Structural and Functional Characteristics of Dyrk, a Novel Subfamily of Protein Kinases with Dual Specificity. *Prog Nucleic Acid Res Mol Biol* **62**, 1–17 (1998).
7. V. Alexandrov, M. Vilenchik, O. Kantidze, N. Tsutskiridze, D. Kharchilava, P. Lhewa, A. Shishkin, Y. Gankin, A. Kirpich, Novel Efficient Multistage Lead Optimization Pipeline Experimentally Validated for DYRK1B Selective Inhibitors. *J Med Chem* **65**, 13784–13792 (2022).
8. A. Barzowska, B. Pucelik, K. Pustelny, A. Matsuda, A. Martyniak, J. Stępniewski, A. Maksymiuk, M. Dawidowski, U. Rothweiler, J. Dulak, G. Dubin, A. Czarna, DYRK1A kinase inhibitors promote β-cell survival and insulin homeostasis. *Cells* **10**, 2263 (2021).
9. E. Deboever, A. Fistrovich, C. Hulme, T. Dunckley, The Omnipresence of DYRK1A in Human Diseases. *International Journal of Molecular Sciences 2022, Vol. 23, Page 9355* **23**, 9355 (2022).
10. J. Wegiel, C. X. Gong, Y. W. Hwang, The role of DYRK1A in neurodegenerative diseases. *FEBS J* **278**, 236–245 (2011).
11. T. Liu, Y. Wang, J. Wang, C. Ren, H. Chen, J. Zhang, DYRK1A inhibitors for disease therapy: Current status and perspectives. *Eur J Med Chem* **229**, 114062 (2022).
12. R. Abbassi, T. G. Johns, M. Kassiou, L. Munoz, DYRK1A in neurodegeneration and cancer: Molecular basis and clinical implications. *Pharmacol Ther* **151**, 87–98 (2015).
13. C. Branca, D. M. Shaw, R. Belfiore, V. Gokhale, A. Y. Shaw, C. Foley, B. Smith, C. Hulme, T. Dunckley, B. Meechoovet, A. Caccamo, S. Oddo, Dyrk1 inhibition improves Alzheimer's disease-like pathology. *Aging Cell* **16**, 1146–1154 (2017).
14. E. Friedman, The Kinase Mirk/dyrk1B: A Possible Therapeutic Target in Pancreatic Cancer. *Cancers 2010, Vol. 2, Pages 1492-1512* **2**, 1492–1512 (2010).
15. X. Deng, S. E. Mercer, C. Y. Sun, E. Friedman, The normal function of the cancer kinase Mirk/dyrk1B is to reduce reactive oxygen species. *Genes Cancer* **5**, 22–30 (2014).
16. H. Chen, J. Shen, E. Choy, F. J. Hornicek, A. Shan, Z. Duan, H. Chen, J. Shen, E. Choy, F. J. Hornicek, A. Shan, Z. Duan, Targeting DYRK1B suppresses the proliferation and migration of liposarcoma cells. *Oncotarget* **9**, 13154–13166 (2017).
17. A. R. Keramati, M. Fathzadeh, G.-W. Go, R. Singh, M. Choi, S. Faramarzi, S. Mane, M. Kasaei, K. Sarajzadeh-Fard, J. Hwa, K. K. Kidd, M. A. Babaee Bigi, R. Malekzadeh, A. Hosseinian, M. Babaei, R. P. Lifton, A. Mani, A Form of the Metabolic Syndrome Associated with Mutations in DYRK1B . *New England Journal of Medicine* **370**, 1909–1919 (2014).
18. C. Ackeifi, E. Swartz, K. Kumar, H. Liu, S. Chalada, E. Karakose, D. K. Scott, A. Garcia-Ocaña, R. Sanchez, R. J. DeVita, A. F. Stewart, P. Wang, Pharmacologic and genetic approaches define human pancreatic β cell mitogenic targets of DYRK1A inhibitors. *JCI Insight* **5** (2020).
19. D. Bossemeyer, The glycine-rich sequence of protein kinases: a multifunctional element. *Trends Biochem Sci* **19**, 201–205 (1994).
20. S. R. Hubbard, Crystal structure of the activated insulin receptor tyrosine kinase in complex with peptide substrate and ATP analog. *EMBO J* **16**, 5572–5581 (1997).
21. D. K. Treiber, N. P. Shah, Ins and Outs of Kinase DFG Motifs. *Chem Biol* **20**, 745–746 (2013).
22. M. Soundararajan, A. K. Roos, P. Savitsky, P. Filippakopoulos, A. N. Kettenbach, J. V. Olsen, S. A. Gerber, J. Eswaran, S. Knapp, J. M. Elkins, Structures of down syndrome kinases, DYRKs, reveal mechanisms of kinase activation and substrate recognition. *Structure* **21**, 986–996 (2013).
23. N. Kannan, A. F. Neuwald, Evolutionary constraints associated with functional specificity of the CMGC protein kinases MAPK, CDK, GSK, SRPK, DYRK, and CK2α. *Protein Science* **13**, 2059–2077 (2004).
24. S. Abu Jhaisha, E. W. Widowati, I. Kii, R. Sonamoto, S. Knapp, C. Papadopoulos, W. Becker, DYRK1B mutations associated with metabolic syndrome impair the chaperone-dependent maturation of the kinase domain. *Scientific Reports 2017 7:1* **7**, 1–13 (2017).

25. M. Rechsteiner, S. W. Rogers, PEST sequences and regulation by proteolysis. *Trends Biochem Sci* **21**, 267–271 (1996).
26. M. Álvarez, X. Estivill, S. de la Luna, DYRK1A accumulates in splicing speckles through a novel targeting signal and induces speckle disassembly. *J Cell Sci* **116**, 3099–3107 (2003).
27. D. Frost, B. Meechoovet, T. Wang, S. Gately, M. Giorgetti, I. Shcherbakova, T. Dunckley, β-Carboline Compounds, Including Harmine, Inhibit DYRK1A and Tau Phosphorylation at Multiple Alzheimer's Disease-Related Sites. *PLoS One* **6**, e19264 (2011).
28. M. F. Lindberg, E. Deau, J. Arfwedson, N. George, P. George, P. Alfonso, A. Corrionero, L. Meijer, Comparative Efficacy and Selectivity of Pharmacological Inhibitors of DYRK and CLK Protein Kinases. *J Med Chem* **66**, 4106–4130 (2023).
29. A. L. Ashford, D. Oxley, J. Kettle, K. Hudson, S. Guichard, S. J. Cook, P. A. Lochhead, A novel DYRK1B inhibitor AZ191 demonstrates that DYRK1B acts independently of GSK3β to phosphorylate cyclin D1 at Thr286, not Thr288. *Biochemical Journal* **457**, 43–56 (2014).
30. J. Hu, H. Deng, E. A. Friedman, Ovarian cancer cells, not normal cells, are damaged by Mirk/Dyrk1B kinase inhibition. *Int J Cancer* **132**, 2258–2269 (2013).
31. S. HIMPEL, P. PANZER, K. EIRMBTER, H. CZAJKOWSKA, M. SAYED, L. C. PACKMAN, T. BLUNDELL, H. KENTRUP, J. GRÖTZINGER, H.-G. JOOST, W. BECKER, Identification of the autophosphorylation sites and characterization of their effects in the protein kinase DYRK1A. *Biochemical Journal* **359**, 497–505 (2001).
32. W. Becker, W. Sippl, Activation, regulation, and inhibition of DYRK1A. *FEBS J* **278**, 246–256 (2011).
33. P. Grygier, K. Pustelny, J. Nowak, P. Golik, G. M. Popowicz, O. Plettenburg, G. Dubin, F. Menezes, A. Czarna, Silmitasertib (CX-4945), a Clinically Used CK2-Kinase Inhibitor with Additional Effects on GSK3β and DYRK1A Kinases: A Structural Perspective. *J Med Chem* **66**, 4009–4024 (2023).
34. J. Chen, E. M. Verheyen, Homeodomain-interacting protein kinase regulates yorkie activity to promote tissue growth. *Current Biology* **22**, 1582–1586 (2012).
35. S. J. H. Wang, D. A. R. Sinclair, H. Y. Kim, S. D. Kinsey, B. Yoo, C. R. Y. Shih, K. K. L. Wong, C. Krieger, N. Harden, E. M. Verheyen, Homeodomain-interacting protein kinase (Hipk) plays roles in nervous system and muscle structure and function. *PLoS One* **15**, e0221006 (2020).
36. D. Dominguez, Y. H. Tsai, R. Weatheritt, Y. Wang, B. J. Blencowe, Z. Wang, An extensive program of periodic alternative splicing linked to cell cycle progression. *Elife* **5** (2016).
37. M. Muraki, B. Ohkawara, T. Hosoya, H. Onogi, J. Koizumi, T. Koizumi, K. Sumi, J. I. Yomoda, M. V. Murray, H. Kimura, K. Furuichi, H. Shibuya, A. R. Krainer, M. Suzuki, M. Hagiwara, Manipulation of alternative splicing by a newly developed inhibitor of Clks. *Journal of Biological Chemistry* **279**, 24246–24254 (2004).
38. N. Bhat, A. Narayanan, M. Fathzadeh, M. Kahn, D. Zhang, L. Goedeke, A. Neogi, R. L. Cardone, R. G. Kibbey, C. Fernandez-Hernando, H. N. Ginsberg, D. Jain, G. I. Shulman, A. Mani, Dyrk1b promotes hepatic lipogenesis by bypassing canonical insulin signaling and directly activating mTORC2 in mice. *J Clin Invest* **132** (2022).
39. C. Noll, C. Planque, C. Ripoll, F. Guedj, A. Diez, V. Ducros, N. Belin, A. Duchon, J. L. Paul, A. Badel, B. de Freminville, Y. Grattau, H. Bléhaut, Y. Herault, N. Janel, J. M. Delabar, DYRK1A, a Novel Determinant of the Methionine-Homocysteine Cycle in Different Mouse Models Overexpressing this Down-Syndrome-Associated Kinase. *PLoS One* **4**, e7540 (2009).
40. Y. Jang, H.-J. Kim, Y. H. Kwon, The involvement of calpain in homocysteine-induced apoptosis in SH-SY5Y cells. *The FASEB Journal* **22**, 877.3-877 (2008).
41. D. E. Koshland, Application of a Theory of Enzyme Specificity to Protein Synthesis. *Proceedings of the National Academy of Sciences* **44**, 98–104 (1958).
42. A. Czarna, J. Wang, D. Zelencova, Y. Liu, X. Deng, H. G. Choi, T. Zhang, W. Zhou, J. W. Chang, H. Kildalsen, O. M. Seternes, N. S. Gray, R. A. Engh, U. Rothweiler, Novel Scaffolds for Dual Specificity Tyrosine-Phosphorylation-Regulated Kinase (DYRK1A) Inhibitors. *J Med Chem* **61**, 7560–7572 (2018).
43. L. Reinhard, H. Mayerhofer, A. Geerlof, J. Mueller-Dieckmann, M. S. Weiss, Optimization of protein buffer cocktails using Thermofluor. *Acta Crystallographica Section F* **69**, 209–214 (2013).
44. W. Kabsch, XDS. *urn:issn:0907-4449* **66**, 125–132 (2010).
45. P. R. Evans, G. N. Murshudov, How good are my data and what is the resolution? *urn:issn:0907-4449* **69**, 1204–1214 (2013).
46. J. Agirre, M. Atanasova, H. Bagdonas, C. B. Ballard, A. Baslé, J. Beilsten-Edmands, R. J. Borges, D. G. Brown, J. J. Burgos-Mármol, J. M. Berrisford, P. S. Bond, I. Caballero, L. Catapano, G. Chojnowski, A. G. Cook, K. D. Cowtan, T. I. Croll, J. Debreczeni, N. E. Devenish, E. J. Dodson, T. R. Drevon, P. Emsley, G. Evans, P. R. Evans, M. Fando, J. Foadi, L. Fuentes-Montero, E. F. Garman, M. Gerstel, R. J. Gildea, K. Hatti, M. L. Hekkelman, P. Heuser, S. W. Hoh, M. A. Hough, H. T. Jenkins, E. Jiménez, R. P. Joosten, R. M. Keegan, N. Keep, E. B. Krissinel, P. Kolenko, O. Kovalevskiy, V. S. Lamzin, D. M. Lawson, A. A. Lebedev, A. G. W. Leslie, B. Lohkamp, F. Long, M. Malý, A. J. McCoy, S. J. McNicholas, A. Medina, C. Millán, J. W. Murray, G. N. Murshudov, R. A. Nicholls, M. E. M. Noble, R. Oeffner, N. S. Pannu, J. M. Parkhurst, N. Pearce, J. Pereira, A. Perrakis, H. R. Powell, R. J. Read, D. J. Rigden, W. Rochira, M. Sammito, F. Sánchez Rodríguez,

G. M. Sheldrick, K. L. Shelley, F. Simkovic, A. J. Simpkin, P. Skubak, E. Sobolev, R. A. Steiner, K. Stevenson, I. Tews, J. M. H. Thomas, A. Thorn, J. T. Valls, V. Uski, I. Usón, A. Vagin, S. Velankar, M. Vollmar, H. Walden, D. Waterman, K. S. Wilson, M. D. Winn, G. Winter, M. Wojdyr, K. Yamashita, The CCP4 suite: integrative software for macromolecular crystallography. *urn:issn:2059-7983* **79**, 449–461 (2023).

47. D. Liebschner, P. V. Afonine, M. L. Baker, G. Bunkoczi, V. B. Chen, T. I. Croll, B. Hintze, L. W. Hung, S. Jain, A. J. McCoy, N. W. Moriarty, R. D. Oeffner, B. K. Poon, M. G. Prisant, R. J. Read, J. S. Richardson, D. C. Richardson, M. D. Sammito, O. V. Sobolev, D. H. Stockwell, T. C. Terwilliger, A. G. Urzhumtsev, L. L. Videau, C. J. Williams, P. D. Adams, Macromolecular structure determination using X-rays, neutrons and electrons: recent developments in Phenix. *urn:issn:2059-7983* **75**, 861–877 (2019).
48. A. J. McCoy, R. W. Grosse-Kunstleve, P. D. Adams, M. D. Winn, L. C. Storoni, R. J. Read, Phaser crystallographic software. *urn:issn:0021-8898* **40**, 658–674 (2007).
49. P. V. Afonine, R. W. Grosse-Kunstleve, N. Echols, J. J. Headd, N. W. Moriarty, M. Mustyakimov, T. C. Terwilliger, A. Urzhumtsev, P. H. Zwart, P. D. Adams, Towards automated crystallographic structure refinement with phenix.refine. *urn:issn:0907-4449* **68**, 352–367 (2012).
50. P. Emsley, B. Lohkamp, W. G. Scott, K. Cowtan, Features and development of Coot. *urn:issn:0907-4449* **66**, 486–501 (2010).
51. O. S. Smart, Sharff A., J. Holstein, T. O. Womack, C. Flensburg, P. Keller, W. Paciorek, C. Vonrhein, Bricogne G., Grade2 version 1.3.0. *Cambridge, United Kingdom: Global Phasing Ltd* (2021).
52. F. Menezes, G. M. Popowicz, ULYSSES: An Efficient and Easy to Use Semiempirical Library for C++. *J Chem Inf Model* **62**, 3685–3694 (2022).
53. F. Menezes, T. Fröhlich, G. M. Popowicz, Can Quantum Chemistry Improve the understanding of Protein-Ligand Interactions? Implications for Structure Based Drug Discovery. *bioRxiv*, 2023.06.01.543295 (2023).
54. C. Bannwarth, S. Ehlert, S. Grimme, GFN2-xTB - An Accurate and Broadly Parametrized Self-Consistent Tight-Binding Quantum Chemical Method with Multipole Electrostatics and Density-Dependent Dispersion Contributions. *J Chem Theory Comput* **15**, 1652–1671 (2019).
55. S. Ehlert, M. Stahn, S. Spicher, S. Grimme, Robust and efficient implicit solvation model for fast semiempirical methods. *J Chem Theory Comput* **17**, 4250–4261 (2021).
56. M. J. Abraham, T. Murtola, R. Schulz, S. Páll, J. C. Smith, B. Hess, E. Lindah, Gromacs: High performance molecular simulations through multi-level parallelism from laptops to supercomputers. *SoftwareX* **1–2**, 19–25 (2015).
57. W. L. Jorgensen, J. Tirado-Rives, Potential energy functions for atomic-level simulations of water and organic and biomolecular systems. *Proc Natl Acad Sci U S A* **102**, 6665–6670 (2005).
58. L. S. Dodda, J. Z. Vilseck, J. Tirado-Rives, W. L. Jorgensen, 1.14∗CM1A-LBCC: Localized Bond-Charge Corrected CM1A Charges for Condensed-Phase Simulations. *Journal of Physical Chemistry B* **121**, 3864–3870 (2017).
59. L. S. Dodda, I. C. De Vaca, J. Tirado-Rives, W. L. Jorgensen, LigParGen web server: an automatic OPLS-AA parameter generator for organic ligands. *Nucleic Acids Res* **45**, W331–W336 (2017).
60. J. Huang, A. D. Mackerell, CHARMM36 all-atom additive protein force field: Validation based on comparison to NMR data. *J Comput Chem* **34**, 2135–2145 (2013).
61. W. L. Jorgensen, J. Chandrasekhar, J. D. Madura, R. W. Impey, M. L. Klein, Comparison of simple potential functions for simulating liquid water. *J Chem Phys* **79**, 926–935 (1983).
62. A. D. MacKerell, D. Bashford, M. Bellott, R. L. Dunbrack, J. D. Evanseck, M. J. Field, S. Fischer, J. Gao, H. Guo, S. Ha, D. Joseph-McCarthy, L. Kuchnir, K. Kuczera, F. T. K. Lau, C. Mattos, S. Michnick, T. Ngo, D. T. Nguyen, B. Prodhom, W. E. Reiher, B. Roux, M. Schlenkrich, J. C. Smith, R. Stote, J. Straub, M. Watanabe, J. Wiórkiewicz-Kuczera, D. Yin, M. Karplus, All-atom empirical potential for molecular modeling and dynamics studies of proteins. *Journal of Physical Chemistry B* **102**, 3586–3616 (1998).
63. J. A. Lemkul, From Proteins to Perturbed Hamiltonians: A Suite of Tutorials for the GROMACS-2018 Molecular Simulation Package [Article v1.0]. *Living J Comput Mol Sci* **1**, 5068–5068 (2019).
64. E. F. Pettersen, T. D. Goddard, C. C. Huang, G. S. Couch, D. M. Greenblatt, E. C. Meng, T. E. Ferrin, UCSF Chimera—A visualization system for exploratory research and analysis. *J Comput Chem* **25**, 1605–1612 (2004).
65. T. D. Goddard, C. C. Huang, E. C. Meng, E. F. Pettersen, G. S. Couch, J. H. Morris, T. E. Ferrin, UCSF ChimeraX: Meeting modern challenges in visualization and analysis. *Protein Science* **27**, 14–25 (2018).
66. E. F. Pettersen, T. D. Goddard, C. C. Huang, E. C. Meng, G. S. Couch, T. I. Croll, J. H. Morris, T. E. Ferrin, UCSF ChimeraX: Structure visualization for researchers, educators, and developers. *Protein Science* **30**, 70–82 (2021).
67. Y. Xie, H. Li, X. Luo, H. Li, Q. Gao, L. Zhang, Y. Teng, Q. Zhao, Z. Zuo, J. Ren, IBS 2.0: an upgraded illustrator for the visualization of biological sequences. *Nucleic Acids Res* **50**, W420–W426 (2022).

Acknowledgements:

We extend our gratitude to Grzegorz Popowicz (Institute of Structural Biology, Helmholtz Zentrum Munchen, Neuherberg, Germany) for his invaluable support, guidance, and scholarly discussions throughout the project. We acknowledge the MCB Structural Biology Core Facility (supported by the TEAM TECH CORE FACILITY/2017-4/6 grant from the Foundation for Polish Science) for valuable support. X-ray data were collected at the HZB BESSY II 14.1 and P11 at DESY. We thank HZB for the allocation of neutron/synchrotron radiation beamtime. We acknowledge DESY (Hamburg, Germany), a member of the Helmholtz Association HGF, for the provision of experimental facilities. Parts of this research were carried out at PETRA III and we would like to thank Johanna Hakanpää for assistance in using beamline P11. Beamtime was allocated for proposal I-20220342 EC.

Funding:

National Science Centre (UMO-2019/34/E/NZ1/00467) to AC
National Science Centre (2022/06/X/NZ1/01418) to KP
NAWA Polish Returns 2018 (PPN/PPO/2018/1/00046/U/00001) to AC

Author contributions:

Conceptualization: PG, KP, FM, AC
Methodology: PG, KP, FM, MJR, PS, AC
Investigation: PG, KP, FM, MJR, PS, AC
Visualization: PG, KP, FM, MJR, PS
Funding acquisition: KP, AC
Project administration: AC
Supervision: AC
Writing—original draft: PG, KP, FM, AC
Writing—review and editing: PG, KP, FM, GD, AC

Competing interests:

The authors declare that they have no competing interests.

Data and materials availability:

Crystal structures of DYRK1B and DYRK1A in complex with AZ191 described in this manuscript are available in PDB (Protein Data Bank; https://www.rcsb.org/) with ID's 8C2Z and 8C3G, respectively. The rest of the data is available in the main text or the supplementary materials.